Materials Advances

Check for updates

Enhanced light driven CO_2 conversion based on silver bismuth sulfide hollow octahedrons coated with amorphous metal–organic frameworks†

Meng-De Dai, Qian Zhang, Hao Dong and Ya-Wen Zhang [ID]*

Ternary sulfides have been widely studied for photocatalytic applications recently due to their flexible chemical composition and feasible band structure regulation. Theoretical research indicates huge potential of $AgBiS_2$ in photocatalysis despite the lack of experimental data. Herein, single crystalline $AgBiS_2$ hollow octahedrons were developed for CO_2 photoreduction with amorphous ZIF-67 frameworks as outer layers. The predominant exposure of (111) planes and central cavities endowed $AgBiS_2$ hollow octahedrons with sufficient light harvesting and electron transfer capability. The core–shell $AgBiS_2$@ZIF-67 heterostructure significantly facilitated the separation of photogenerated carriers on the interface and electron accumulation around the active sites, further inducing stronger electrostatic attraction between ZIF-67 and ruthenium bipyridine complexes as photosensitizers. In consequence, $AgBiS_2$@ZIF-67 heterostructures with medium thickness of outer layers exhibited the optimum photo-catalytic efficiency towards CO_2 photoreduction with the average CO and H_2 production rates of 2.27 mmol g_{cat}^{-1} h^{-1} and 0.78 mmol g_{cat}^{-1} h^{-1}, which qualified $AgBiS_2$ hollow octahedrons as a univer-sal platform for cocatalyst loading in heterogeneous catalysis.

Introduction

The efficient storage and utilization of solar energy for carbon dioxide conversion to renewable chemical fuels ought to be a major approach to alleviate current environmental problems, such as energy crisis and greenhouse effect.[1–6] Thanks to superior generation rate of photoexcited electrons compared to inorganic semiconductors, ruthenium bipyridine complexes are commonly exploited as photosensitizers with cobalt or rhenium complexes as cocatalysts to optimize the utilization of solar energy and improve the efficiency of photocatalytic process.[7–11] Apart from photosensitizers and cocatalysts, suitable bridging ligands or supports can be essential for boosting the electron transfer process as well as stabilizing the active sites.[12–18] For heterogenous catalysis, it is basically unfavorable for photoinduced electrons to follow a direct path from photo-sensitizers to cocatalysts in a dilute solution as charge transfer usually requires two complexes in close proximity to each other.

Hence, a rational design of supports can make a huge impact on the charge transfer behavior between photosensitizers and cocatalysts.[12,17,19]

It is well established that metal sulfide semiconductors with narrow band gaps normally have advantages in light harvesting and charge transfer in heterogenous catalysis. Though some catalysts are incapable of performing the photocatalytic reac-tion independently due to insufficient band gaps, the introduc-tion of ruthenium and cobalt complexes can effectively compensate for the drawbacks of metal sulfides.[5,6] Meanwhile, binary metal sulfides have been thoroughly studied to date and further investigation on sulfide-based photocatalysts should focus on the fabrication of ternary and quaternary sulfides, such as $CuGaS_2$, $CuIn_5S_8$, $ZnIn_2S_4$ and Cu_2ZnSnS_4, which might contribute to the discovery of materials with novel morphology and distinct band structure.[20–23] Recently, $AgBiS_2$ nanocrystals have been found to possess extremely high absorption coeffi-cient and thus applied to sensitized solar cells with positive results.[24,25] As an earth-abundant and non-toxic ternary metal sulfide, $AgBiS_2$ can absorb most of the light in the visible region and generate adequate electrons under mild conditions.[26–31] It is therefore reasonable to speculate that $AgBiS_2$ should have great potential in CO_2 photoreduction.[31–33]

Herein, for the very first time, we present an octahedron-shaped $AgBiS_2$ hollow nanostructure coated with a thin layer of ZIF-67 frameworks as the cocatalyst for a typical CO_2

Beijing National Laboratory for Molecular Sciences, State Key Laboratory of Rare Earth Materials Chemistry and Applications, PKU-HKU Joint Laboratory in Rare Earth Materials and Bioinorganic Chemistry, College of Chemistry and Molecular Engineering, Peking University, Beijing 100871, China.
E-mail: ywzhang@pku.edu.cn; Fax: +86-10-62756787; Tel: +86-10-62756787
† Electronic supplementary information (ESI) available: More data on TEM images, PXRD and XPS analyses, and photocatalytic measurements of hetero-structures. See DOI: https://doi.org/10.1039/d3ma00662j

photoreduction reaction driven by $[Ru(bpy)_3]^{2+}$ as the photosensitizers. In this case, $AgBiS_2$ hollow octahedrons (ABS-HO) substantially served as a neutral platform for loading Co(II) active sites and assisting the adsorption of aqueous $[Ru(bpy)_3]^{2+}$ ions at the same time, which promoted not only the reaction rate but also the long-term stability. Notably, hollow octahedron nanostructures included two apparent characters: existence of central cavities and major exposure of {111} facets. On the one hand, large cavities enabled multiple reflections and scattering of incident light, which was beneficial to sufficient utilization of solar energy.[34–36] On the other hand, (111) polar terminations solely consisting of Ag or S atoms were expected to exhibit a metallic character and hence able to provide an ideal interface for initial accumulation and subsequent transfer process of photo-induced electrons, as revealed by first-principles studies.[33] In short, ABS-HO should be competent to function as a photoactive support for potential cocatalysts. To our knowledge, ZIF-67 frameworks contained multiple coordinatively unsaturated metal sites and specialized in CO_2 conversion to CO under visible light illumination, which were thus selected to load onto the surface of ABS-HO for enhanced physical and chemical adsorption of CO_2 molecules.[37–39] To explore the specific charge transfer behavior at the interface of core–shell $AgBiS_2$@ZIF-67 nanocrystals, various characterization methods were applied and based on the experimental results it could be inferred that the significantly improved photocatalytic performance of $AgBiS_2$@ZIF-67 heterostructures resulted from the extraordinary photoelectrochemical properties of ABS-HO cores as well as boosted charge separation efficiency on the interface.

Experimental section

Chemicals

$AgNO_3$ (A.R., Xilong Chemical Co., Ltd), $Co(NO_3)_2·6H_2O$ (A.R., Xilong Chemical Co., Ltd), $Bi(NO_3)_3·5H_2O$ (A.R., Beijing Mreda Technology Co., Ltd), thiourea (A.R., TCI Development Co., Ltd), KBr (A.R., Xilong Chemical Co., Ltd), 2-methylimidazole (A.R., Sinopharm Chemical Reagent Co., Ltd), poly(vinylpyrrolidone) (M.W. = 30 000, Aladdin Reagent Co., Ltd), $Ru(bpy)_3Cl_2·6H_2O$ (98%, Aladdin Reagent Co., Ltd), triethanolamine (A.R., Beijing Tongguang Fine Chemical Co., Ltd), acetonitrile (A.R., Tianjin Concord Technology Co., Ltd), methanol (A.R., Tianjin Concord Technology Co., Ltd) and ethylene glycol (A.R., Tianjin Concord Technology Co., Ltd) were used without further purification.

Synthesis of ABS-HO

The novel $AgBiS_2$ hollow octahedrons were prepared by a facile solvothermal method, in which nitrate salts and thiourea were used as the metal source and sulfur source respectively. In a typical procedure, 60 mg of $AgNO_3$, 170 mg of $Bi(NO_3)_3·5H_2O$ and 500 mg of PVP were first dissolved in 20 mL of ethylene glycol. Subsequently, 20 mL of ethylene glycol containing 70 mg of thiourea and 10 mL of ethylene glycol containing 240 mg of KBr were added to the above solution successively with stirring until a transparent pale-yellow solution was formed. The mixture

was immediately transferred to a 100 mL Teflon-lined autoclave reactor and then placed in an oven at 180 °C for 20 min, 40 min, 60 min, 80 min, 100 min, 120 min and 24 h, which corresponded to a series of samples denoted as ABS-20, ABS-40, ABS-60, ABS-80, ABS-100, ABS-120 and ABS-HO. The products were collected by centrifugation and then washed three times by deionized water and ethanol. The precipitates were dried at 70 °C overnight and ground into fine powders for further use.

Synthesis of ZIF-67 and core–shell heterostructures

40 mg of ABS-HO was initially dispersed in 16 mL of methanol with 400 mg of 2-methylimidazole by sonication. Subsequently, 4 mL of methanol containing 10 mg, 20 mg and 40 mg of $Co(NO_3)_2·6H_2O$ was added to the above suspension. The mixture was continuously stirred for 24 h at room temperature. The products (denoted as AZ-10, AZ-20 and AZ-40) were collected through centrifugation and then washed three times with ethanol. The precipitates were dried at 70 °C overnight and ground into fine powders for further use.

For the preparation of ZIF-67, 400 mg of 2-methylimidazole was dissolved in 16 mL of methanol followed by the addition of 4 mL of methanol with 80 mg of $Co(NO_3)_2·6H_2O$ while the remaining steps were the same as above.

Electrochemical measurements

The electrochemical measurements were all carried out on an electrochemical workstation (CHI760e, CH Instruments) using a standard three-electrode system, which included platinum foil, KCl-saturated Ag/AgCl and carbon paper with catalysts as the counter electrode, reference electrode and working electrode, respectively. The working electrodes were prepared as follows: 5 mg of catalysts were first dispersed in Nafion ethanol solution (0.5 wt%, 1 mL) by sonication. The suspension was added onto a piece of carbon paper (1 × 2 cm^2) dropwise under an infrared lamp until solvent vaporized completely. Mott–Schottky (MS) plots were measured at the frequency of 500 Hz with the potential from −1.5 V to 1.5 V (vs. Ag/AgCl) using 0.5 M Na_2SO_4 aqueous solution as the electrolyte. Electrochemical impedance spectroscopy (EIS) experiments were performed at 0 V (vs. Ag/AgCl) ranging from 0.1 Hz to 1 MHz with an amplitude of 5 mV using 0.1 M $KHCO_3$ aqueous solution as the electrolyte. Periodic photocurrent responses with on/off cycles were recorded at 0 V (vs. Ag/AgCl) under the irradiation of a Xe lamp (ca. 100 mW cm^{-2}, Beijing Perfectlight Technology) with a UV cutoff filter ($\lambda > 400$ nm) using 0.1 M $KHCO_3$ aqueous solution as the electrolyte.

Photocatalytic CO_2 reduction

The photocatalytic performance of samples was evaluated by a CO_2 reduction reaction performed on a photocatalytic system (Labsolar-IIIAG, Beijing Perfectlight Technology) with a borosilicate glass photoreactor. In a typical procedure, 20 mg of $Ru(bpy)_3Cl_2·6H_2O$ and 2 mg of cocatalysts were uniformly dispersed in 12 mL of deionized water by sonication. The homogenous suspension was immediately transferred to the photoreactor together with 12 mL of triethanolamine (TEOA)

and 36 mL of acetonitrile (MeCN) under constant stirring. The test temperature was maintained at 15 °C by circulating cooling water. In order to ensure the complete exclusion of oxygen, the sealed system was continuously purged with CO_2 (99.999%) for 60 min before light irradiation. Subsequently, the photoreactor was placed under a 300 W Xe lamp with a UV cutoff filter ($\lambda >$ 400 nm). During the photocatalytic tests, possible gaseous products were determined by an online gas chromatograph (GC-7806, Beijing Shiweipx Analysis Instrument) using Ar as the carrier gas. CO and CH_4 were both detected by a flame ionization detector while H_2 was detected by a thermal conductivity detector. The liquid products were analyzed by hydrogen-1 nuclear magnetic resonance (^{1}H NMR) spectroscopy.

Instrumentation

The morphology of nanostructures was investigated by transmission electron microscopy (TEM), high-resolution transmission electron microscopy (HRTEM) and high-angle annular dark-field scanning transmission electron microscopy (HAADF-STEM) on an FEG-TEM (JEM-2100F, JEOL). The elemental distribution of nanostructures was analyzed by energy-dispersive X-ray (EDX) spectroscopy. Field-emission scanning electron microscopy (FESEM) was adopted to verify the spatial configuration of nanostructures using a scanning electron microscope (S-4800, Hitachi). The crystalline phases of samples were determined by powder X-ray diffraction patterns (PXRD) on an X-ray diffractometer (D/MAX-2000, Rigaku). The UV-vis-NIR diffuse reflectance spectra (DRS) were recorded on a UV-vis-NIR spectrometer (UV-3600 Plus, Shimadzu) with pure barium sulfates as the background. Fourier transform infrared spectra (FTIR) were measured on a Fourier transform infrared spectrometer (Nicolet iS50, Thermo Fisher) with the KBr pallet technique. The Ag : Bi : Co molar ratios of samples were obtained by inductively coupled plasma objective emission spectroscopy (ICP-OES) on an ICP-OES spectrometer (Prodigy, Leeman). The oxidation states of constituent elements in the as-prepared samples were determined by X-ray photoelectron spectroscopy (XPS) on an X-ray photoelectron spectrometer (AXIS Supra, Shimadzu) with Al Kα radiation. All the XPS binding energy values were calibrated by the C 1s peaks of surface adventitious carbon at 284.8 eV. The possible mechanism of electron migration was studied by steady-state photoluminescence spectroscopy (PL) on a fluorescence spectrometer (FLS980, Edinburgh Instruments) at room temperature.

Results and discussion

Characterization of ABS-HO

Cubic $AgBiS_2$ hollow octahedrons were fabricated through a template-free solvothermal method, in which thiourea and ethylene glycol were selected as the sulfur source and solvent, as illustrated in Fig. 1a. TEM and SEM images display the distinct morphology of hollow octahedron shaped $AgBiS_2$ nanocrystals, as shown in Fig. 1b. The lattice fringes with a spacing of 0.200 nm measured in the HRTEM image should be ascribed to the (220) lattice planes of cubic $AgBiS_2$ (Fig. 1c). The selected
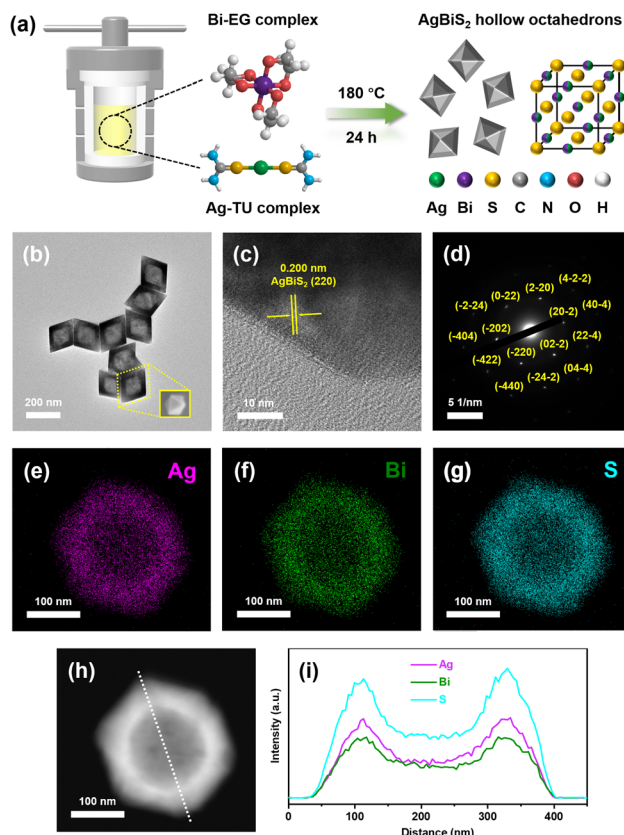

Fig. 1 (a) The schematic diagram for the solvothermal synthesis process of ABS-HO. (b) TEM and SEM (inset) images, (c) HRTEM image, (d) SAED pattern and (e)–(h) HAADF-STEM with EDX elemental mapping images of a single hollow octahedral nanostructure. (i) The elemental distribution of ABS-HO along the dashed line denoted in (h).

area electron diffraction (SAED) pattern clearly proves the single crystalline character of ABS-HO (Fig. 1d). HAADF-STEM and EDX elemental mapping images demonstrate the uniform distribution of constituent elements (Ag, Bi and S) in a single hollow octahedron without any observable segregation in sight (Fig. 1e–h). Hence, undesired formation of impurity phases including Ag_2S and Bi_2S_3 can be excluded from the solvothermal synthesis. The EDX elemental line scanning profile confirms the existence of cavities inside ABS-HO. The average edge lengths for octahedrons and cavities were *ca.* 185 nm and 120 nm (Fig. 1i).

According to first-principles studies, Wulff shaped $AgBiS_2$ inclines to expose not only (100) type nonpolar surfaces but also (111) type polar terminations, which further leads to the morphology of truncated cubes in theory.[33] In terms of catalyst design, predominant exposure of polar surfaces can significantly improve the adsorption and mobilization of both photoactive and photoinactive species, including reactants, photosensitizers and cocatalysts. Since {111} crystal facets are close packed planes solely consisting of either Ag, Bi or S atoms, the hollow octahedron shaped nanostructure undoubtedly maximizes polar terminations with high surface energy, which should be conducive to potential catalytic applications.
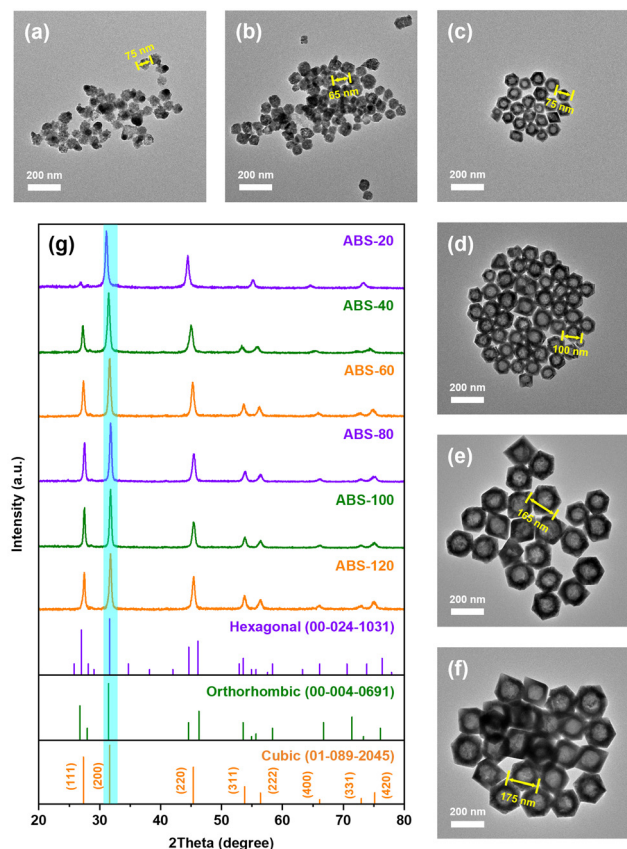
Fig. 2 TEM images of (a) ABS-20 (nuclei), (b) ABS-40 (particles), (c) ABS-60, (d) ABS-80, (e) ABS-100 and (f) ABS-120. (g) PXRD patterns of AgBiS$_2$ prepared in time sequence.

To fulfill the most exposure of polar surfaces, KBr and PVP were both indispensable for the anisotropic growth of ABS-HO. Inspired by the controllable synthesis of silver nanocubes, Br$^-$ ions and PVP molecules were introduced in the EG-based system to regulate the growth kinetics of AgBiS$_2$ nanocrystals.[40–42] In consequence, additive agents effectively altered the growth rates of nanostructures along ⟨100⟩ and ⟨111⟩ directions through the selective interaction with different crystallographic planes. Notably, the (111) polar terminations might show active chemical properties under ambient conditions despite the fact that ABS-HO was the most stable species in the reaction medium.

In order to unravel the evolution mechanism during the solvothermal reaction, a series of AgBiS$_2$ nanocrystals were prepared in time sequence, as shown in Fig. 2a–f. The aggregates observed in ABS-20 were at least 60 nm in size, which were composed of multiple primary nuclei. The basic polyhedron units with rough edges began to appear in ABS-40 with an approximate size of 60–70 nm. Subsequently, with progressive sharpening of edges and corners, the octahedron shaped nanostructures first came into existence in ABS-60. Within the next hour, hollow octahedrons continued to enlarge with interior cavities, whose edge lengths ranged from ca. 75 nm to 175 nm.

The characteristic diffraction peaks in PXRD patterns of samples are basically consistent with standard AgBiS$_2$ patterns of the cubic phase (01-089-2045), further confirming the phase

purity during the entire crystal growth process (Fig. 2g). However, it is worth noting that a slight shift of diffraction peaks toward lower angles can be found in the patterns of ABS-20 and ABS-40, which presumably originate from small-sized nanocrystals with partial lattice expansion. The relative intensities of the diffraction peak at 27.5° in correspondence with {111} facets also appear to be much lower for ABS-20 and ABS-40 than other samples. This phenomenon demonstrates that primary nuclei with poorer crystallinity and enlarged d-spacing suffer from serious atomic disorder on the {111} facets, probably due to non-metal doping.[43] By contrast, the diffraction peaks of other samples simply coincide with the standard pattern. Since close packed (111) planes are highly ordered atomic layers, predominant exposure of (100) planes at the early stage of crystal growth should be a kinetically driven result. It can be inferred that Br doping mainly occurs at the nucleation and aggregation stage followed by slow anion substitution during the remaining reaction time.

To confirm this view, high resolution XPS spectra of ABS-20, ABS-60, ABS-120 and ABS-HO were measured to determine the oxidation states of constituent elements. The XPS spectra of Ag 3d, Bi 4f, S 2p and Br 3d regions are demonstrated in Fig. 3a–c. In the Bi 4f spectra overlapping with the S 2p region, two strong peaks appear at 162.6 eV and 157.3 eV for ABS-120 and ABS-HO. The corresponding peaks emerge at 162.7 eV and 157.4 eV for ABS-60. In addition to two major peaks at 163.3 eV and 158.0 eV, a pair of satellite peaks can be observed at 164.3 eV and 159.0 eV for ABS-20, which derives from the antisite defects of Bi atoms in the primary nuclei.[26,27] As presented in the same spectra, two weak peaks at 161.4 eV and 160.3 eV belong to S 2p$_{1/2}$ and S 2p$_{3/2}$ of S^{2-} for ABS-120 and ABS-HO, which shift to 161.5 eV and 160.4 eV for ABS-60. The corresponding peaks further shift to 161.9 eV and 160.8 eV for ABS-20. The Ag 3d spectra show doublet peaks at 372.8 eV and 366.8 eV for
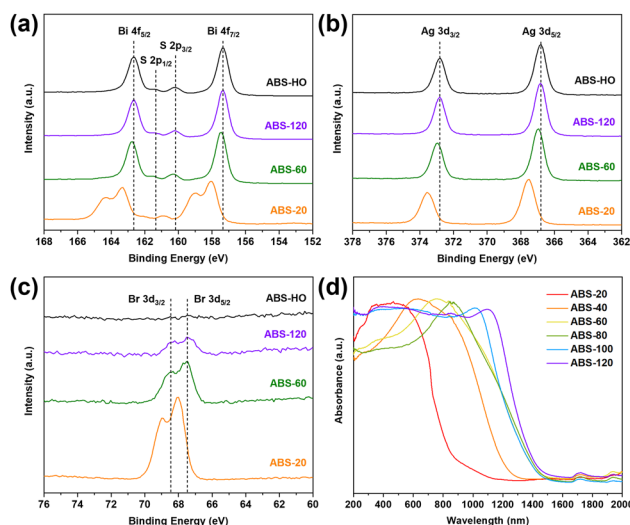

Fig. 3 High-resolution XPS spectra of (a) Bi 4f overlapping with S 2p region, (b) Ag 3d region and (c) Br 3d region of ABS-20, ABS-60, ABS-120 and ABS-HO. (d) UV-vis-NIR diffuse reflectance spectra of AgBiS$_2$ prepared in time sequence.

ABS-120 and ABS-HO, which should be assigned to Ag 3d$_{3/2}$ and Ag 3d$_{5/2}$ of Ag$^+$.[26,27] The peaks observed in the Ag 3d spectra of ABS-60 are located at 372.9 eV and 366.9 eV, further shifting to 373.5 eV and 367.5 eV for ABS-20. In general, the oxidation states of Ag, Bi and S can be regarded as +1, +3 and −2 based on the above results except for ABS-20. It is also worth mentioning that ABS-60 shows slightly higher binding energies than ABS-120 and ABS-HO. As for the Br 3d spectra, the relative intensities of peaks monotonically decrease with the extension of reaction time and eventually vanish in the spectra of ABS-HO. Hence, a certain conclusion can be drawn that Br doping can make a significant impact on the formation of AgBiS$_2$ nuclei, directly inducing atomic defects and lower electron density around Ag, Bi and S atoms. This phenomenon can be attributed to the particular competition between slow release S^{2-} ions from thiourea and excess Br$^-$ ions in the solution. Considering the much lower solubility of AgBiS$_2$, S substitution should be favorable in thermodynamics.

Despite the above constituent elements, characteristic peaks of C, N and O can be also detected in the XPS spectra (Fig. S1 in the ESI†), indicating strong adsorption of PVP molecules on the surface of AgBiS$_2$ nanocrystals. In addition, FTIR spectra can confirm the existence of PVP molecules as well (Fig. S2 in ESI†). The broad absorption band ranging from 3600 cm^{-1} to 3000 cm^{-1} evidently belongs to the stretching vibration of O–H bonds from water molecules adsorbed on the surface. The absorption peaks located at 2916 cm^{-1}, 1652 cm^{-1}, 1437 cm^{-1} and 1274 cm^{-1} can be attributed to the vibration of C–H bonds, C=O bonds, methylene groups (–CH$_2$–) and peptide bonds (–CO–NH–).[42] On account of XPS and FTIR spectra, PVP molecules attached to the (111) planes of AgBiS$_2$ nanocrystals should be considered irremovable during the solvothermal reaction while doped Br$^-$ ions can easily dissolve back into the solution through anion exchange.

The optical properties of AgBiS$_2$ nanocrystals with different sizes were thoroughly investigated *via* UV-vis-NIR diffuse reflectance spectroscopy (Fig. 3d). Basically, AgBiS$_2$ nanocrystals can absorb most of light in the ultraviolet and visible region. However, the absorption edges gradually shift toward the near infrared region as the reaction time prolongs. This monotonic trend is in accordance with TEM images and PXRD patterns of corresponding samples. In other words, the uncommon behavior of ABS-20 and ABS-40 simply arises from the small-sized character of nanocrystals, which causes not only poorer crystallinity but also enlarged band gaps thanks to the quantum confinement effect. By comparison, AgBiS$_2$ nanocrystals obtained from 60 min to 120 min have homologous structural and optical properties. Notably, every single spectrum can be transformed to the corresponding Tauc plot by using a conversion formula: $(\alpha h\nu)^{1/r} = C(h\nu - E_g)$, where α, h, ν and C represent the absorption coefficient, Planck constant, frequency of incident light and proportional constant. The r value should be 1/2 for direct semiconductors or 2 for indirect semiconductors. The consequent band gap values can be then approximated by extrapolating the linear region to the abscissa. Regarding AgBiS$_2$ as an indirect band gap semiconductor,[32] the corresponding band gaps of ABS-20, ABS-40, ABS-60, ABS-80,

ABS-100 and ABS-120 ought to be 1.20 eV, 0.90 eV, 0.77 eV, 0.76 eV, 0.75 eV and 0.75 eV (Fig. S3 in ESI†). It is clear that the quantum confinement effect primarily influences ABS-20 and ABS-40 as kinetically driven products.

To unravel the mechanism of crystal growth, several control experiments were conducted for the crystal growth process without various additive agents. TEM images display that AgBiS$_2$ nanorods were generated for both circumstances in the absence of KBr or PVP (Fig. S4 in ESI†). Hence, it is reasonable to presume that Br$^-$ ions and PVP molecules can stabilize (111) planes after initial nuclei self-assemble into basic polyhedrons. In detail, doped Br$^-$ ions should be distinguished from adsorbed Br$^-$ ions regarding their functions in facet control. During the nucleation and aggregation process, Br$^-$ ions doped in the lattices of AgBiS$_2$ nanocrystals evidently tend to suppress the selective growth of close packed (111) planes according to PXRD patterns. By contrast, Br$^-$ ions adsorbed on the surface can lower the energy of (111) planes with Ag or Bi terminations by electrostatic attraction.

On the one hand, small-sized adsorbates are easier to remove by deionized water and ethanol than long-chain macromolecules, which explains the fact that C, N and O show characteristic peaks in the XPS spectra of ABS-HO while signal of Br cannot be detected. On the other hand, it is more accessible for Br$^-$ ions to interact with small-sized nuclei than PVP molecules at the beginning of crystal growth.[26,27,41] The nucleation process involves the participation of Br$^-$ ions, which limits the concentration of free Ag$^+$ ions in the solution and therefore inhibits the overall reaction.[41] Meanwhile, deficient S^{2-} ions endow Br$^-$ ions with chances of doping in the lattice as counter ions. It is worth noting that doped Br$^-$ ions can easily detach from the lattice without affecting the phase purity of cubic AgBiS$_2$.

Based on the structural and elemental analyses of samples, a plausible evolution mechanism can be proposed, as presented in Fig. 4. First, rapid nucleation induces partial Br doping in the cubic AgBiS$_2$ lattices and further influences the diffraction peaks in the PXRD pattern. Owing to the strong passivation of Br$^-$ ions, subsequent growth basically depends on anion exchange in the solution, which conduces to the formation of small aggregates at this stage. The aggregates incline to assemble into basic polyhedron units by oriented attachment rather than grow directly through Ostwald ripening.[44] As edges and corners of polyhedron units are sharpened progressively, neighbouring pores will naturally converge into a central cavity. Since enlarged cavities lead to more exposure of (111) planes, continuous growth of hollow octahedrons should be a thermodynamically favorable result. This process perhaps involves anion transfer from the inner side to the outer surface through the lattices followed by deposition with cations.

Characterization of core–shell heterostructures

Single crystalline cubic AgBiS$_2$ hollow octahedrons are exploited as cocatalysts for CO$_2$ photoreduction when ZIF-67 outer shells with different thicknesses were loaded onto the surface of ABS-HO. TEM and HRTEM images of AZ-20 demonstrate that an
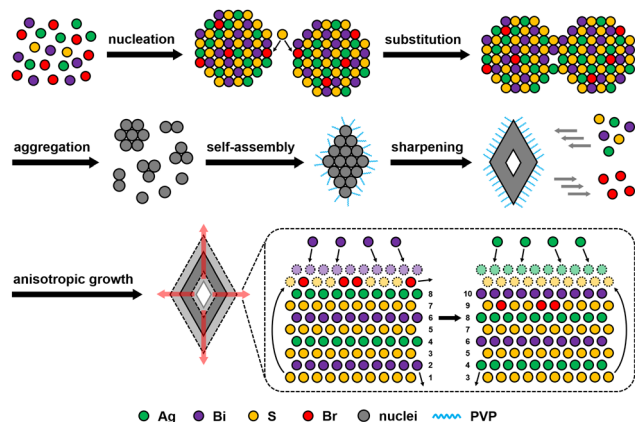
Fig. 4 Schematic diagram for the plausible crystal growth mechanism of ABS-HO.

outer layer of ZIF-67 (*ca.* 10–20 nm in thickness) was successfully coated on ABS-HO as an external extension of the original octahedron, where Co and N disperse uniformly in the region of nearly amorphous ZIF-67 frameworks (Fig. 5a–i). To further determine the elemental distribution of AZ-20 from the interior core to the outer shell, HAADF-STEM and EDX elemental line scanning were applied to visualize the chemical composition inside a single octahedron nanostructure (Fig. S5 in ESI†). Apparently, Co and N both have detective signals beyond the ABS-HO core, proving the construction of core–shell heterostructure.

In addition, TEM images of AZ-10, AZ-40 and ZIF-67 were also captured for comparison (Fig. S6 in ESI†). The outer shell of AZ-20 appears to be thicker than AZ-10 and thinner than AZ-40 while ZIF-67 shows the typical morphology of rhombic

dodecahedra. According to the PXRD patterns, the characteristic diffraction peaks of as-prepared ZIF-67 are consistent with the simulated pattern. The relative intensities of diffraction peaks within the small angle region increase slightly from AZ-10 to AZ-40, suggesting poor crystallinity of ZIF-67 on the shell (Fig. S7 in ESI†).[45] FTIR spectra confirm the existence of 2-methylimidazole in AZ-20 and ZIF-67 with no obvious signal of PVP (Fig. S8 in ESI†).[38,45] Furthermore, ICP-OES was performed to determine the actual contents of Co in different samples. In consequence, the approximate values of Ag : Bi : Co molar ratios in AZ-10, AZ-20 and AZ-40 were 1 : 1 : 0.2, 1 : 1 : 0.4 and 1 : 1 : 0.9, respectively.

UV-vis-NIR diffuse reflectance spectra clarify that the optical properties of ABS-HO and ZIF-67 substantially remain unchanged in the core–shell heterostructures (Fig. S9 in ESI†). The absorption peaks of ABS-HO and ZIF-67 are located at 1125 nm and 586 nm respectively, corresponding to band gaps of 0.75 eV and 1.98 eV, as revealed by Tauc plots (Fig. S10 in ESI†). Mott–Schottky tests were conducted to uncover more details about band structures of ABS-HO, AZ-20 and ZIF-67 (Fig. 6a). The curve slope of ABS-HO appears to be positive with classical n-type semiconductor characteristics while ZIF-67 shows negative curve slope with typical p-type semiconductor characteristics. The Mott–Schottky plot of AZ-20 possesses both characteristics of ABS-HO and ZIF-67, verifying the composition of two semiconductors in the core–shell heterostructures. The flat band potential can be acquired by extrapolating the linear region to the abscissa. The position of valence band maximum (VBM) can be estimated to the flat band potential for ZIF-67 as a p-type semiconductor. Likewise, the position of the conduction band minimum (CBM) can be obtained by the estimation based on the Mott–Schottky plot for n-type semiconductors.
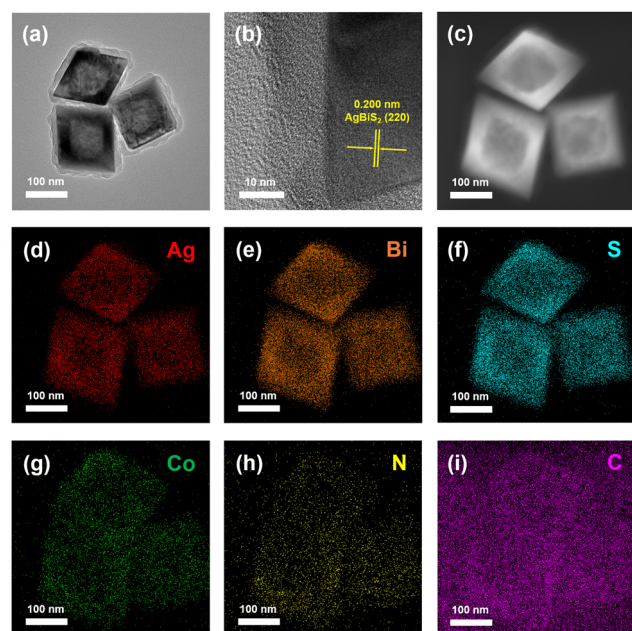

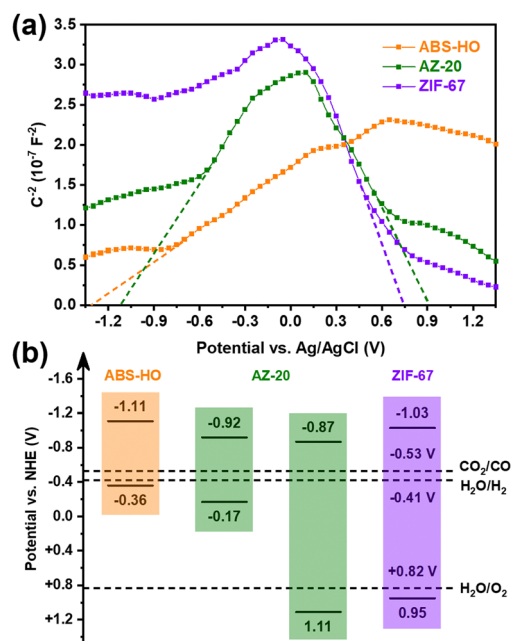Fig. 5 (a) TEM image, (b) HRTEM image and (c)–(i) HAADF-STEM with EDX elemental mapping images of AZ-20.

Fig. 6 (a) Mott–Schottky plots and (b) schematic diagram for the band alignment of ABS-HO, AZ-20 and ZIF-67.

The relative positions of VBM and CBM in ABS-HO, AZ-20 and ZIF-67 are summarized in Fig. 6b according to Tauc plots and Mott–Schottky plots. Undoubtedly, AZ-20 should be categorized as a type-II heterostructure and thus favorable for photogenerated electrons to transfer from the ABS-HO core to the ZIF-67 shell.[1–4] High resolution XPS spectra were also measured to determine the direction of electron migration between ABS-HO and ZIF-67 (Fig. S11 in ESI†). In the Ag 3d and Bi 4f spectra, peaks shift to higher binding energy with the increasing content of Co, reflecting an inevitable loss of electron density. By comparison, the binding energy of Co almost remains unchanged for all the samples, revealing the steady oxidation state of +2 for Co. The binding energy of N slightly decreases from AZ-10 to ZIF-67. On account of the Fermi levels, electrons should migrate from ABS-HO to ZIF-67 spontaneously. In practice, two components seem to both suffer from electron deficiency when mixed together. This phenomenon could be ascribed to the desorption of PVP and partial oxidation of 2-methylimidazole.

Photocatalytic CO_2 reduction performance

The photocatalytic performance was substantially evaluated by CO_2 photoreduction, where MeCN and H_2O were employed as solvent for CO_2 while triethanolamine (TEOA) served as the sacrificial agent. The volume ratio of MeCN/H_2O/TEOA mixture was $3:1:1$ for all the tests to fulfill the optimum photocatalytic conditions with the introduction of $Ru(bpy)_3Cl_2$ as photosensitizers. Though the mixed solution remained homogenous at the beginning, phase separation would inevitably occur upon CO_2 saturation. The upper solution with the majority of neutral CO_2 molecules was pale-orange while the lower solution with $Ru(bpy)_3Cl_2$ and CO_2-TEOA zwitterions was scarlet.[46]

During the photocatalytic tests, CO was the only carbonaceous reduction product with H_2 as the by-product derived from the decomposition of water under light irradiation. The experimental results are in accordance with previous reports regarding CO_2 conversion to CO initiated by Ru(ɪɪ)–Co(ɪɪ) complexes.[10,12,36] $Ru(bpy)_3Cl_2$ can hardly trigger CO_2 photoreduction reaction in the absence of cocatalysts despite its high photoexcitation efficiency. By contrast, Co(ɪɪ) complexes are practically incapable of utilizing solar energy in exchange for excited electrons. In other words, the catalytic performance of Ru(ɪɪ)–Co(ɪɪ) complexes mostly depends on the transfer rate of electrons from Ru(ɪɪ) sites to Co(ɪɪ) sites.

In consequence, all of the cocatalysts can convert CO_2 into CO molecules with the side reaction of hydrogen evolution except for ABS-HO showing the worst catalytic performance, which implies that Co(ɪɪ) complexes should be responsible for the adsorption and activation of substrate molecules (Fig. 7a and b). However, pure ZIF-67 with theoretically more active sites shows a lower production rate than AZ-10, AZ-20 and AZ-40. In detail, AZ-20 as the best catalyst produced 54.4 µmol CO and 17.8 µmol H_2 in total, which were collected during the photocatalytic test with reaction time extended to 12 h for the demonstration of superior stability. It is worth mentioning that AZ-20 and ABS-HO can work in the reaction medium
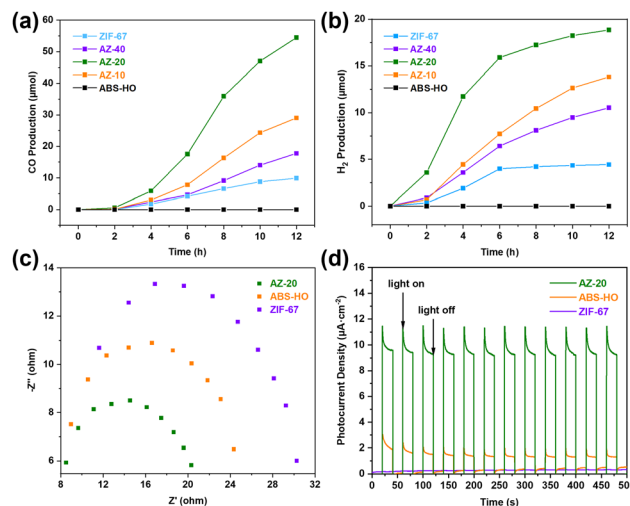

Fig. 7 Time-dependent (a) CO and (b) H_2 productions of ABS-HO, AZ-10, AZ-20, AZ-40 and ZIF-67. (c) EIS Nyquist plots and (d) transient photocurrent spectra of ABS-HO, AZ-20 and ZIF-67.

continuously with basic nanostructures unchanged, as presented in TEM images (Fig. S12 in ESI†). PXRD patterns were recorded to determine the phase purity of AZ-20 after the photocatalytic test as well (Fig. S13 in ESI†). It is well established that $Ru(bpy)_3Cl_2$ would inevitably suffer from photobleaching under visible light irradiation. Hence, Ru(ɪɪ)–Co(ɪɪ) complexes normally function in a short test before stepwise deactivation causes serious efficiency decay.[36,38] Since the rate of CO production remained steady for 12 hours, $Ru(bpy)_3Cl_2$ ought to be more stable when coupled with AZ-20 in the solution. Suppressed decomposition of $Ru(bpy)_3Cl_2$ could originate from strong attachment to the supports, which stabilizes the chromospheres on the photosensitizers.[12]

EIS Nyquist plots and periodic photocurrent responses were recorded to explore the carrier migration kinetics of cocatalysts (Fig. 7c and d). Among these samples, AZ-20 shows the smallest arc radius of the Nyquist plot, which represents lower charge transfer impedance and more advantageous charge transfer kinetics. By comparison, pure ZIF-67 nanocrystals with much higher impedance should have great difficulty in carrier migration. Likewise, AZ-20 also exhibits the highest photocurrent density whilst the periodic photocurrent responses of ZIF-67 can be hardly detected under the same test conditions. Therefore, ZIF-67 can barely make any contribution to either light harvesting or charge transfer under light illumination while ABS-HO as the inner core can generate and transport numerous electrons to the surface of ZIF-67 as the outer shell, further inducing strong photocurrent in AZ-20.

The average production rates of all the samples are presented in Fig. 8a for further comparison. To further investigate the origin of optimum photocatalytic performance for AZ-20, steady-state PL spectra were recorded to simulate the process of electron migration under light illumination (Fig. 8b). Upon the irradiation of monochronic incident light (450 nm), certain cocatalysts dispersed in the MeCN/TEOA/H_2O solution with $Ru(bpy)_3Cl_2$ will emit strong fluorescence detected by the
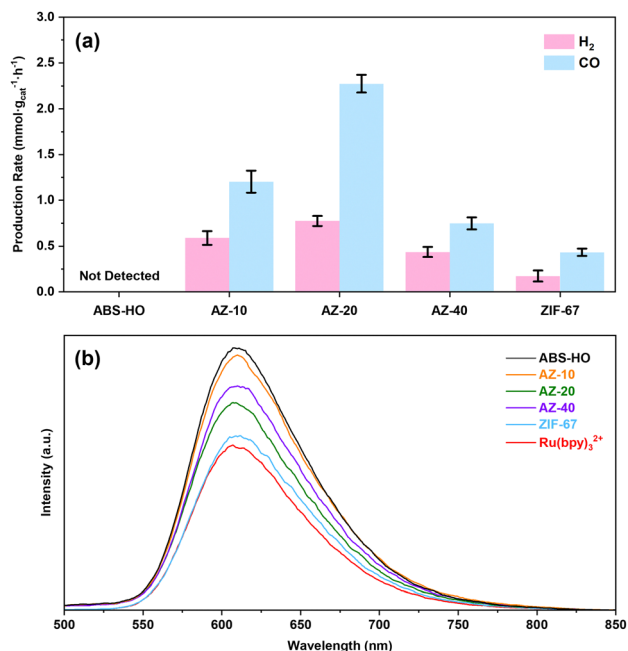
Fig. 8 (a) The average CO and H_2 production rates and (b) steady state PL spectra of ABS-HO, AZ-10, AZ-20, AZ-40 and ZIF-67.
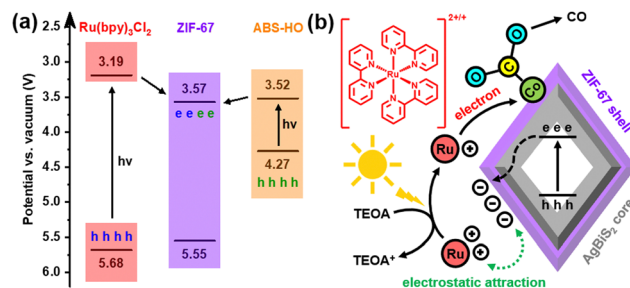

Fig. 9 Schematic diagrams for (a) the transfer process of photoinduced electrons between $Ru(bpy)_3Cl_2$ and core–shell heterostructures and (b) the plausible mechanism of CO_2 photoreduction reaction triggered by $Ru(bpy)_3Cl_2$ and AZ-20.

instrument. Interestingly, sole $Ru(bpy)_3Cl_2$ without the assistance of cocatalysts shows the lowest fluorescence intensity. The fluorescence emission of $[Ru(bpy)_3]^{2+}$ ions reaches the climax when coupled with ABS-HO. Furthermore, AZ-10, AZ-20 and AZ-40 can also enhance the characteristic fluorescence from $[Ru(bpy)_3]^{2+}$ in the solution. The relative intensity of fluorescence emission for AZ-20 appears to be lower than AZ-10 and AZ-40, which can accord with the photocatalytic performance as decay of fluorescence intensity should be mainly ascribed to electron transfer from $[Ru(bpy)_3]^{2+}*$ to Co(II) sites. Hence, an outer shell with medium thickness can endow the catalyst with both abundant active sites on the surface and photoexcited electrons from the inner core.

In terms of mass transfer, it should be unfeasible for TEOA and $[Ru(bpy)_3]^{2+}$ to reach the ABS-HO core through small pores of ZIF-67 frameworks in the heterostructures.[17] Naturally, Co(II) sites on the surface ought to be responsible for the adsorption and activation of substrates or photosensitizers. The electron migration process can only occur on the interface between cores and shells or on the surface of ZIF-67 with adsorbed photosensitizers while direct charge transfer between ABS-HO and $[Ru(bpy)_3]^{2+}$ should be inaccessible. It is worth mentioning that even AZ-40 with the thickest outer layers shows stronger fluorescence than sole $[Ru(bpy)_3]^{2+}$, confirming that the ABS-HO core mainly affects $[Ru(bpy)_3]^{2+}$ by electron transfer rather than electric field or energy transfer. In other words, photo-electrons generated by ABS-HO would accumulate on the surface of ZIF-67 and provide a negative environment for the adsorption of $[Ru(bpy)_3]^{2+}$ ions by electrostatic attraction. Considering that the fluorescence intensity of $[Ru(bpy)_3]^{2+}$ barely changes upon the addition of ZIF-67, direct electron transfer from aqueous $[Ru(bpy)_3]^{2+}$ ions to the surface of p-type ZIF-67

should be unfavorable. By contrast, the negative surfaces created by ABS-HO at the photoexcited state can easily facilitate the adsorption of free $[Ru(bpy)_3]^{2+}$ ions in the solution and thus inhibit the quenching process induced by collision, further leading to enhanced fluorescence of $[Ru(bpy)_3]^{2+}$. Based on the band alignment and charge transfer kinetics, a plausible mechanism for electron transfer process is illustrated in Fig. 9a and b.

It should be mentioned that none of the samples can trigger the reaction without photosensitizers and negligible reduction products were collected during the tests. Meanwhile, all of the photocatalysts are inactive in the absence of CO_2, TEOA and light irradiation, which means no detection of products under a nitrogen-protected atmosphere, sacrificial agent-free system or/and dark conditions (Fig. S14 in ESI†). $Ru(bpy)_3Cl_2$ as the sole photocatalyst exhibits relatively low CO production rate with high selectivity towards H_2 evolution instead. ^{1}H NMR spectra also clarify that none of the liquid reduction products were obtained during the aforementioned photocatalytic tests (Fig. S15 in ESI†). Basically, the pale-orange upper solution after the reaction was acetonitrile solution containing $Ru(bpy)_3Cl_2$, TEOA and H_2O whilst the scarlet lower solution was $Ru(bpy)_3Cl_2$ aqueous solution mixed with TEOA and MeCN.

To sum up, ABS-HO should have remarkable potential in the regulation and optimization of active sites for different catalyst units. In this work, suitable band alignment leads to the construction of core–shell heterostructures based on cubic ABS-HO nanocrystals and amorphous ZIF-67 frameworks with enhanced photocatalytic performance, thanks to boosted carrier transfer through the type-II heterostructure. During the photocatalytic reaction, ABS-HO effectively promotes not only the reduction ability of potential cocatalysts but also the stability of expensive photosensitizers.

Conclusion

Single crystalline cubic $AgBiS_2$ hollow octahedrons were fabricated for the first time by a facile solvothermal method. The time-dependent morphology and elemental analyses of $AgBiS_2$ crystals revealed a novel mechanism for the anisotropic growth of hollow nanostructures. During the solvothermal synthesis, Br^- ions and PVP molecules are both responsible for regulating

the growth rates of different facets through selective interaction. As an earth-abundant and non-toxic sulfide support, ABS-HO can absorb most of the light in the visible region and provide the cocatalysts with sufficient photogenerated electrons to create a negative surface for subsequent adsorption and activation of substrates and photosensitizers. In this work, the optimum core–shell heterostructure AZ-20 with medium thickness of ZIF-67 outer layers exhibited superior photocatalytic performance with the average CO and H_2 production rates of 2.27 mmol g_{cat}^{-1} h^{-1} and 0.78 mmol g_{cat}^{-1} h^{-1}. The enhanced photocatalytic efficiency and stability should be mainly attributed to optimal utilization of solar energy and boosted separation of photogenerated carriers, which derives from the unique structural and photoelectrochemical properties of ABS-HO and rational construction of the type-II heterostructure. Hopefully, ABS-HO can serve as a universal platform for loading potential cocatalyst units and inspire further studies on ternary sulfides as well as hollow nanostructures in the future.

Conflicts of interest

The authors declare no conflicts of interest.

Acknowledgements

Notes and references

1 W. Tu, Y. Zhou and Z. Zou, Photocatalytic conversion of CO_2 into renewable hydrocarbon fuels: State-of-the-art accomplishment, challenges, and prospects, *Adv. Mater.*, 2014, **26**, 4607.

2 H. Li, Y. Zhou, W. Tu, J. Ye and Z. Zou, State-of-the-art progress in diverse heterostructured photocatalysts toward promoting photocatalytic performance, *Adv. Funct. Mater.*, 2015, **25**, 998.

3 X. Li, J. Yu and M. Jaroniec, Hierarchical photocatalysts, *Chem. Soc. Rev.*, 2016, **45**, 2603.

4 J. Low, J. Yu, M. Jaroniec, S. Wageh and A. A. Al-Ghamdi, Heterojunction photocatalysts, *Adv. Mater.*, 2017, **29**, 1601694.

5 J. Wang, S. Lin, N. Tian, T. Ma, Y. Zhang and H. Huang, Nanostructured metal sulfides: Classification, modification strategy, and solar-driven CO_2 reduction application, *Adv. Funct. Mater.*, 2021, **31**, 2008008.

6 Q. Zhu, Q. Xu, M. Du, X. Zeng, G. Zhong, B. Qiu and J. Zhang, Recent progress of metal sulfide photocatalysts for solar energy conversion, *Adv. Mater.*, 2022, **34**, 2202929.

7 K. Kobayashi, T. Kikuchi, S. Kitagawa and K. Tanaka, Selective generation of formamides through photocatalytic CO_2 reduction catalyzed by ruthenium carbonyl compounds, *Angew. Chem., Int. Ed.*, 2014, **53**, 11813–11817.

8 X. Yang, T. Liang, J. Sun, M. J. Zaworotko, Y. Chen, P. Cheng and Z. Zhang, Template-directed synthesis of photocatalyst-encapsulating metal–organic frameworks with boosted photocatalytic activity, *ACS Catal.*, 2019, **9**, 7486–7493.

9 H. Zhang, J. Wei, J. Dong, G. Liu, L. Shi, P. An, G. Zhao, J. Kong, X. Wang, X. Meng, J. Zhang and J. Ye, Efficient visible-light-driven carbon dioxide reduction by a single-atom implanted metal–organic framework, *Angew. Chem., Int. Ed.*, 2016, **55**, 14310–14314.

10 H. Liu, F. Zhang, H. Wang, J. Xue, Y. Guo, Q. Qian and G. Zhang, Oxygen vacancy engineered unsaturated coordination in cobalt carbonate hydroxide nanowires enables highly selective photocatalytic CO_2 reduction, *Energy Environ. Sci.*, 2021, **14**, 5339–5346.

11 K. M. Choi, D. Kim, B. Rungtaweevoranit, C. A. Trickett, J. T. D. Barmanbek, A. S. Alshammari, P. Yang and O. M. Yaghi, Plasmon-enhanced photocatalytic CO_2 conversion within metal–organic frameworks under visible light, *J. Am. Chem. Soc.*, 2017, **139**, 356–362.

12 T. Hirose, Y. Maeno and Y. Himeda, Photocatalytic carbon dioxide photoreduction by $Co(bpy)_3^{2+}$ sensitized by $Ru(bpy)_3^{2+}$ fixed to cation exchange polymer, *J. Mol. Catal. A: Chem.*, 2003, **193**, 27–32.

13 G. Sahara, H. Kumagai, K. Maeda, N. Kaeffer, V. Artero, M. Higashi, R. Abe and O. Ishitani, Photoelectrochemical reduction of CO_2 coupled to water oxidation using a photocathode with a Ru(II)–Re(I) complex photocatalyst and a CoOx/TaON photoanode, *J. Am. Chem. Soc.*, 2016, **138**, 14152–14158.

14 A. M. Cancelliere, F. Puntoriero, S. Serroni, S. Campagna, Y. Tamaki, D. Saito and O. Ishitani, Efficient trinuclear Ru(II)–Re(I) supramolecular photocatalysts for CO_2 reduction based on a new tris-chelating bridging ligand built around a central aromatic ring, *Chem. Sci.*, 2020, **11**, 1556–1563.

15 D. Saito, Y. Yamazaki, Y. Tamaki and O. Ishitani, Photocatalysis of a dinuclear Ru(II)–Re(I) complex for CO_2 reduction on a solid surface, *J. Am. Chem. Soc.*, 2020, **142**, 19249–19258.

16 J. Tian, Y. Zhang, L. Du, Y. He, X.-H. Jin, S. Pearce, J.-C. Eloi, R. L. Harniman, D. Alibhai, R. Ye, D. L. Phillips and I. Manners, Tailored self-assembled photocatalytic nanofibres for visible-light-driven hydrogen production, *Nat. Chem.*, 2020, **12**, 1150–1156.

17 P. M. Stanley, J. Haimerl, C. Thomas, A. Urstoeger, M. Schuster, N. B. Shustova, A. Casini, B. Rieger, J. Warnan and R. A. Fischer, Host–Guest interactions in a metal–organic framework isoreticular series for molecular photocatalytic CO_2 reduction, *Angew. Chem., Int. Ed.*, 2021, **60**, 17854–17860.

18 Q. Zhang, S. Gao, Y. Guo, H. Wang, J. Wei, X. Su, H. Zhang, Z. Liu and J. Wang, Designing covalent organic frameworks with Co-O₄ atomic sites for efficient CO_2 photoreduction, *Nat. Commun.*, 2023, **14**, 1147.

19 J. Zhang, S. Shao, D. Zhou, T. Di and T. Wang, Two-dimensional layered Co(OH)$_2$/g-C$_3$N$_4$/Ni(OH)$_2$ ternary nano-composites for enhanced visible-light photocatalytic H$_2$-production activity, *ACS Appl. Energy Mater.*, 2021, **4**, 6340–6347.

20 T. M. Suzuki, S. Yoshino, T. Takayama, A. Iwase, A. Kudo and T. Morikawa, Z-Schematic and visible-light-driven CO$_2$ reduction using H$_2$O as an electron donor by a particulate mixture of a Ru-complex/(CuGa)$_{1-x}$Zn$_{2x}$S$_2$ hybrid catalyst, BiVO$_4$ and an electron mediator, *Chem. Commun.*, 2018, **54**, 10199–10202.

21 X. Li, Y. Sun, J. Xu, Y. Shao, J. Wu, X. Xu, Y. Pan, H. Ju, J. Zhu and Y. Xie, Selective visible-light-driven photocatalytic CO$_2$ reduction to CH$_4$ mediated by atomically thin CuIn$_5$S$_8$ layers, *Nat. Energy*, 2019, **4**, 690–699.

22 S. Wang, B. Y. Guan, Y. Lu and X. W. D. Lou, Formation of hierarchical In$_2$S$_3$–CdIn$_2$S$_4$ heterostructured nanotubes for efficient and stable visible light CO$_2$ reduction, *J. Am. Chem. Soc.*, 2017, **139**, 17305–17308.

23 K. Kim, A. Razzaq, S. Sorcar, Y. Park, C. A. Grimes and S.-I. In, Hybrid mesoporous Cu$_2$ZnSnS$_4$ (CZTS)–TiO$_2$ photo-catalyst for efficient photocatalytic conversion of CO$_2$ into CH$_4$ under solar irradiation, *RSC Adv.*, 2016, **6**, 38964–38971.

24 M. Bernechea, N. Cates, G. Xercavins, D. So, A. Stavrinadis and G. Konstantatos, Solution-processed solar cells based on environmentally friendly AgBiS$_2$ nanocrystals, *Nat. Photonics*, 2016, **10**, 521–525.

25 Y. Wang, S. R. Kavanagh, I. Burgués-Ceballos, A. Walsh, D. O. Scanlon and G. Konstantatos, Cation disorder engi-neering yields AgBiS$_2$ nanocrystals with enhanced optical absorption for efficient ultrathin solar cells, *Nat. Photonics*, 2022, **16**, 235–241.

26 P. Lei, R. An, X. Zheng, P. Zhang, K. Du, M. Zhang, L. Dong, X. Gao, J. Feng and H. Zhang, Ultrafast synthesis of ultra-small polyethylenimine-protected AgBiS$_2$ nanodots by "roo-kie method" for in vivo dual-modal CT/PA imaging and simultaneous photothermal therapy, *Nanoscale*, 2018, **10**, 16765–16774.

27 S. Wen, T. Wu, H. Long, L. Ke, S. Deng, L. Huang, J. Zhang and S. Tan, Mechanism insight into rapid photodriven sterilization based on silver bismuth sulfide quantum dots, *ACS Appl. Mater. Interfaces*, 2021, **13**, 21979–21993.

28 B. Chen, C. Zhang, W. Wang, Z. Chu, Z. Zha, X. He, W. Zhou, T. Liu, H. Wang and H. Qian, Ultrastable AgBiS$_2$ hollow nanospheres with cancer cell-specific cytotoxicity for multi-modal tumor therapy, *ACS Nano*, 2020, **14**, 14919–14928.

29 E. Gu, X. Lin, X. Tang, G. J. Matt, A. Osvet, Y. Hou, S. Jäger, C. Xie, A. Karl, R. Hock and C. J. Brabec, Single molecular precursor ink for AgBiS$_2$ thin films: Synthesis and charac-terization, *J. Mater. Chem. C*, 2018, **6**, 7642–7651.

30 S. Sugarthi, R. Roshanchandrapal, T. R. Naveenkumar, G. Bakiyaraj, M. Navaneethan, J. Archana, S. Harish and B. Neppolian, Synthesis and characterization of AgBiS$_2$/rGO nanocomposites: Interfacial charge transfer process, *Mater. Lett.*, 2021, **302**, 130416.

31 Q. Chen, Y. Ma, B. Qi, T. Zhang, L. Wang, J. Shi and X. Lan, Z-scheme Bi/AgBiS$_2$/P25 for enhanced CO$_2$ photoreduction to CH$_4$ and CO with photo-thermal synergy, *Appl. Surf. Sci.*, 2021, **555**, 149648.

32 F. Viñes, M. Bernechea, G. Konstantatos and F. Illas, Matil-dite versus schapbachite: First-principles investigation of the origin of photoactivity in AgBiS$_2$, *Phys. Rev. B*, 2016, **94**, 235203.

33 F. Viñes, G. Konstantatos and F. Illas, Matildite contact with media: First-principles study of AgBiS$_2$ surfaces and nanoparticle morphology, *J. Phys. Chem. B*, 2018, **122**, 521–526.

34 M.-C. Tsai, J.-Y. Lee, P.-C. Chen, Y.-W. Chang, Y.-C. Chang, M.-H. Yang, H.-T. Chiu, I.-N. Lin, R.-K. Lee and C.-Y. Lee, Effects of size and shell thickness of TiO$_2$ hierar-chical hollow spheres on photocatalytic behavior: An experi-mental and theoretical study, *Appl. Catal., B*, 2014, **147**, 499–507.

35 J.-Y. Lee, M.-C. Tsai, P.-C. Chen, T.-T. Chen, K.-L. Chan, C.-Y. Lee and R.-K. Lee, Thickness effects on light absorption and scattering for nanoparticles in the shape of hollow spheres, *J. Phys. Chem. C*, 2015, **119**, 25754–25760.

36 Y. Su, Z. Song, W. Zhu, Q. Mu, X. Yuan, Y. Lian, H. Cheng, Z. Deng, M. Chen, W. Yin and Y. Peng, Visible-light photo-catalytic CO$_2$ reduction using metal-organic framework derived Ni(OH)2 nanocages: A synergy from multiple light reflection, static charge transfer, and oxygen vacancies, *ACS Catal.*, 2021, **11**, 345–354.

37 J. Qin, S. Wang and X. Wang, Visible-light reduction CO$_2$ with dodecahedral zeolitic imidazolate framework ZIF-67 as an efficient co-catalyst, *Appl. Catal., B*, 2017, **209**, 476–482.

38 X. Yuan, Q. Mu, S. Xue, Y. Su, Y. Zhu, H. Sun, Z. Deng and Y. Peng, Polypyrrole reinforced ZIF-67 with modulated facet exposure and billion-fold electrical conductivity enhance-ment towards robust photocatalytic CO$_2$ reduction, *J. Energy Chem.*, 2021, **60**, 202–208.

39 M. Wang, J. Liu, C. Guo, X. Gao, C. Gong, Y. Wang, B. Liu, X. Li, G. G. Gurzadyan and L. Sun, Metal–organic frame-works (ZIF-67) as efficient cocatalysts for photocatalytic reduction of CO$_2$: The role of the morphology effect, *J. Mater. Chem. A*, 2018, **6**, 4768–4775.

40 Y. Sun and Y. Xia, Shape-controlled synthesis of gold and silver nanoparticles, *Science*, 2002, **298**, 2176–2179.

41 A. Ruditskiy and Y. Xia, Toward the synthesis of sub-15 nm Ag nanocubes with sharp corners and edges: The roles of heterogeneous nucleation and surface capping, *J. Am. Chem. Soc.*, 2016, **138**, 3161–3167.

42 Y. Liu, Y. L. Balachandran, D. Li, Y. Shao and X. Jiang, Polyvinylpyrrolidone–poly(ethylene glycol) modified silver nanorods can be a safe, noncarrier adjuvant for HIV vac-cine, *ACS Nano*, 2016, **10**, 3589–3596.

43 I. Shown, S. Samireddi, Y.-C. Chang, R. Putikam, P.-H. Chang, A. Sabbah, F.-Y. Fu, W.-F. Chen, C.-I. Wu, T.-Y. Yu, P.-W. Chung, M. C. Lin, L.-C. Chen and K.-H. Chen, Carbon-doped SnS$_2$ nanostructure as a high-efficiency

solar fuel catalyst under visible light, *Nat. Commun.*, 2018, **9**, 169.

44 B. Li and H. C. Zeng, Architecture and preparation of hollow catalytic devices, *Adv. Mater.*, 2019, **31**, 1801104.

45 C. Hu, J. Xu, Y. Wang, M. Wei, Z. Lu and C. Cao, Core–shell crystalline ZIF-67@amorphous ZIF for high-performance supercapacitors, *J. Mater. Sci.*, 2020, **55**, 16360–16373.

46 R. N. Sampaio, D. C. Grills, D. E. Polyansky, D. J. Szalda and E. Fujita, Unexpected roles of triethanolamine in the photochemical reduction of CO_2 to formate by ruthenium complexes, *J. Am. Chem. Soc.*, 2020, **142**, 2413–2428.